Small Signal Modeling and Decoupled Controller Design for a Triple Active Bridge Multiport DC–DC Converter

Ishita Biswas, *Student Member, IEEE*, Debaprasad Kastha, *Senior Member, IEEE*, and Prabodh Bajpai, *Senior Member, IEEE*

***Abstract*—This article proposes modeling and two controller design techniques for a triple active bridge (TAB) three-port dc–dc converter comprising of fuel cell, battery, and load. The sources are integrated, employing boost interleaved full-bridge converters in order to get smoother source current profile. The converter is a nonlinear multi-input multi-output (MIMO) system with a large number of control variables. Moreover, a high degree of coupling among the control variables makes its modeling and control system design quite cumbersome and complex. To overcome the complexity of analysis in a higher order system like TAB, a generalized frequency-domain modeling technique is introduced in this article. A new decoupling matrix-based proportional-integral controller design method is also proposed. It reduces the design complexity and improves the system dynamic performance (lower settling time, overshoot/undershoot in the controlled variables) in comparison to similar three-port converters reported in the literature. Further, the performance of the proposed controller is compared by simulation with another popular MIMO system controller design technique, namely the state feedback control. A 1-kW laboratory prototype is built and tested to verify the system performance during dynamic load changes, source current variation, and battery charging/discharging operation.**

***Index Terms*—Decoupled control, frequency domain analysis, multiport converter (MPC), soft switching, small signal model, triple active bridge (TAB).**

I. Introduction

DC RENEWABLE energy sources and storage devices are conventionally interfaced using separate single or multistage power electronic converters in dc microgrids (DCMG). But the main drawbacks of such arrangements are low efficiency due to an increased number of conversion stages (particularly between the sources and the energy storage devices), high cost of the system due to a larger number of active switches along with complex communication requirement, voltage oscillation, and complicated protection requirement. To solve these problems, the multiport converter (MPC) technology can be a desirable solution as they allow interconnection of different sources [photovoltaic, fuel cell (FC), etc.] and storage devices [battery, supercapacitor (SC)] at varying voltage levels with bidirectional power flow capability in a compact single converter structure with centralized control [1]. Thus, they reduce the number of redundant conversion stages and elaborate communication requirements of conventional DCMG structures. MPCs are becoming increasingly popular in applications such as hybrid vehicles, satellite communication, microgrids, uninterpretable power supplies, etc. [2]. For applications requiring high voltage conversion ratio, transformer-isolated MPC topologies are beneficial, as the transformer turns ratios can be adjusted to achieve the desired voltage gain. Among the topologies available for isolated MPCs, dual active bridge derived converter topologies have been a popular choice as they feature advantages, such as higher source utilization, isolation, bidirectional power flow, and wide soft-switching range [3]–[5]. Further, triple active bridge (TAB) based converter topologies are also gaining interest [6], [7], specifically for multiport power converter applications. They are realized using three bidirectional active bridges (half-bridge/full-bridge converter) integrated by a single high frequency (HF) three winding transformer [8], which naturally makes provision for at least two source integration.

TAB can be voltage fed (VF-TAB) [9], [10], current fed (CF-TAB) [11]–[13] or of hybrid structure (combination of both voltage and CF ports) [14]. Among them, VF-TABs (both half bridge and full bridge) and CF triple active half-bridge (CF-TAHB) topologies, where one or more ports are boost integrated half-bridge modules, have been most extensively studied by researchers so far. In case of TABs, there exists maximum five degrees of freedom for modulation namely, three active bridges duty ratios/inner phase shift angles, and two phase shift angles among the transformer voltages. VF-TABs have been a popular choice so far among the researchers. But, none so far, have considered the variation of all five control variables. In case of sources with wide voltage variation, duty ratio control is mandatory in order to maintain the transformer winding voltage levels at their respective rated designed values. In this respect, CF-TAB is a better alternative to VF-TAB, especially for storage integration, due to its ability to handle wide input voltage variation with duty ratio control, lower source current ripple, and wide soft-switching region. Many CF-TAHB topologies have

Manuscript received January 22, 2020; revised May 18, 2020; accepted June 21, 2020. Date of publication July 2, 2020; date of current version September 22, 2020. Recommended for publication by Associate Editor J. He. *(Corresponding author: Ishita Biswas.)*

The authors are with the Department of Electrical Engineering, Indian Institute of Technology Kharagpur, Kharagpur 721302, India (e-mail: i.biswas4@gmail.com; kastha@ee.iitkgp.ac.in; pbajpai@ee.iitkgp.ac.in).

Color versions of one or more of the figures in this article are available online at https://ieeexplore.ieee.org.

Digital Object Identifier 10.1109/TPEL.2020.3006782

been reported in the literature where one or more ports are boost integrated half-bridge modules [11]–[14]. However, there are some limitations of CF-TAHB based topologies such as, high switch, and transformer current stress (for high power applications), higher input current ripple, large circulating current, etc. Further, it produces asymmetrical transformer voltage levels (in half-bridge CF ports, for duty ratio other than 50%) which may cause transformer voltage mismatch if all three bridges are not switched at the same duty ratio. In this regard, full-bridge CF-TAB can be a promising candidate for high power MPC applications. Since in this case, the transformer voltages remain symmetrical irrespective of the duty ratio variation, which helps in extending the soft switching range. It also reduces the transformer winding and switch current rating compared to the CF-TAHB. This article mainly focuses on the detailed modeling and control of full bridge CF-TAB converters for high power MPC applications.

Depending on the converter structure (full bridge/half-bridge), a huge number of operating modes are possible for TABs considering its full control flexibility. This makes time-domain analysis of the converter, exceedingly complicated even in steady-state since the power flow equations change depending on the operating mode and the range of phase shift angles. Therefore, unified frequency domain analysis [15] has to be used to formulate the steady-state system equations. In this regard, the most popular approach for TAB-based system modeling is the conventional state-space averaging technique. This approach has been quite popular for TAB modeling in general [12], [16]–[18]. To model the individual controllers, the power flow equations are linearized to form independent single-input single-output systems by introducing feedforward decoupling compensation. Proportional integral derivative (PID) compensators are then used to control these SISO systems. This approach has already been used in several VF-TAB converters for decoupling the control loops of the phase shift angles [19]–[22]. Similar approach can be used for modeling and design decoupled controller for CF-TAB converters also. In [12], the duty cycle and phase shift controller bandwidths were chosen in such a way so that their coupling effects become negligible. But the approach presented is very much parameter and control objective specific, which limits its utility in case of wide input voltage variation. The work in [13] designs the phase shift controller bandwidth to be sufficiently low, to avoid coupling. But this article is limited to phase shift controller design only. In [14] also, a dynamically decoupled power flow controller is designed neglecting the coupling effect among the phase shift and duty ratio controllers. All the abovementioned modeling techniques, are formulated for CF-TAHB converters only, from which it is difficult to draw a clear incite into the generalized modeling technique for CF-TAB. Further, in these modeling techniques the power equations are formulated based on first harmonic approximations, where the higher order harmonics of the square/quasi square wave transformer voltages are neglected. This can lead to significant computational error in converter modeling.

The available system modeling and controller design techniques for CF-TAHB, are typically limited to phase shift modulation only, neglecting the effect of duty ratio variation of each active bridges. Some authors have worked on the modeling of the converter considering more than two control variables. In [15], a variable duty ratio, variable frequency modulation is employed for a VF-TAB converter. In [11], a CF-TAHB structure was proposed, where two CF half-bridge circuits integrate a battery and a SC. However, a fixed 50% duty ratio control, implemented for the CF ports, causes loss of soft switching during wide battery/SC voltage variation. This converter was modulated by asymmetrical duty ratio plus phase-shift control in [12]. In this case, a lower value of the filter inductor improves the soft-switching range but causes a higher source current ripple. In [14], only one boost half-bridge was employed for storage integration, while the other two ports still retained VF structure. In this case, both VF and CF ports are controlled by the same duty ratio (generated for the CF the port) to ensure voltage matching. But, this modulation limits the power transfer capability of the VF ports.

In the cited literature most of the controller design and modeling techniques are limited to specific converter structure operating modes and modulation strategy. To the best of the knowledge of the authors, no full-bridge CF-TAB converter modeling and controller design has been studied so far, considering its full control flexibility. In view of the above limitations, the objective of this article is to develop a unified powerful modeling and controller design technique for the full-bridge CF-TAB converter, considering all degrees of freedom. Here, two boost interleaved CF ports integrate a FC and a battery to the load which is connected at the dc side of a full-bridge VF port. The full-bridge interleaved structure plays a key role in achieving a wide soft-switching range with source current ripple cancellation. In order to incorporate all possible operating modes, a pulsewidth modulation (PWM) plus phase-shift modulation is implemented for the full-bridge CF-TAB, to operate over a wide input voltage range. The duty ratio variation of each active bridges, generates quasi-square wave voltages across the transformer windings, which helps to increase soft switching range of the converter [23]. The major contributions of this article can be summarized as follows:

1) A frequency domain steady-state model for the full-bridge CF-TAB is proposed considering higher order harmonics of the transformer voltage waveforms. This model is independent of the transformer voltage profile, while the available TAB models are applicable for square wave transformer voltages only. Further the proposed model overcomes the error involved with the available first harmonic approximated modeling techniques by considering higher order harmonics.
2) The proposed generalized steady-state model is further used to formulate state-space model of the full bridge CF-TAB converter. Since the model includes all control variables, the state-space model is generic for the entire range of operating modes and modulation strategies. In contrast, most of the modeling and control techniques reported in the literature assume the converter to be operating in a specific mode with a given modulation strategy.
3) Based on the abovementioned state-space model, a detailed small signal modeling of the converter is carried out

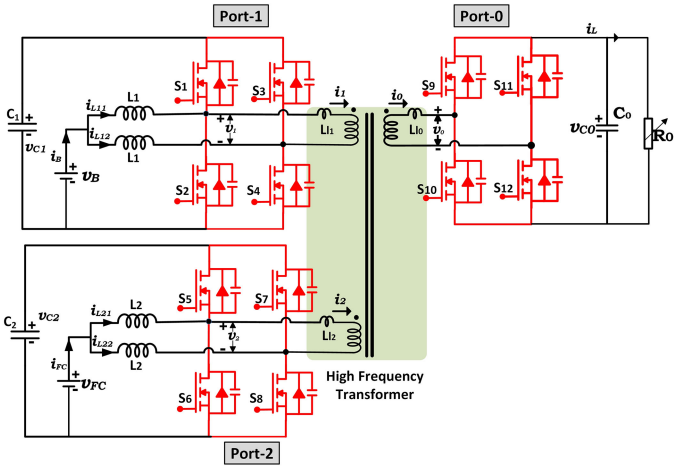

Fig. 1. TAB-based MPC structure.

which finally reduces to ac equivalent circuits for each of the three ports. A general method for decoupling these equivalent circuits is also proposed, which significantly simplifies the individual controller design. Similar decoupling controllers have been proposed in the literature before. However, they have invariably been specific to a particular modulation strategy.

The organization of the rest of this article is as follows. Section II describes the topology and operating principle of the converter. The generalized frequency domain steady-state model is established here along with the derivation of power flow equations. In Section III, a detailed state-space small-signal average model of the CF-TAB is derived. Based on this, two different controllers namely the state feedback controller and the proportional integral (PI)-based decoupled controller is designed in detail. The performance of the proposed decoupled controller is compared with that of the state feedback controller by simulation in Section IV. Performance of the proposed PI-based decoupled controller is experimentally validated on a laboratory prototype in Sections V. Finally, Section VI concludes this article.

II. System Configuration and Performance Analysis

A. Topology Description

The topology of the proposed CF-TAB-based MPC is shown in Fig. 1. It consists of three bidirectional ports, among which two input ports (Port-1 and Port-2) are used to integrate a battery and an FC, respectively. Each of them is constructed as two-phase boost interleaved CF circuits using two identical parallel inductors (L_1 for Port-1), and (L_2 for Port-2), which reduces individual switch current stress and smooths the input current drawn from the sources. Input side CF structure also helps to extend the soft-switching range of the input side bridges by proper choice of the boost inductors L_1, L_2 [23]. The full-bridge VF structure at the output port (Port-0) is directly coupled with the load side dc bus capacitor. A HF three winding transformer interconnects these three individual ports with electrical isolation and voltage matching among the clamp capacitors (C_1, C_2, C_0).

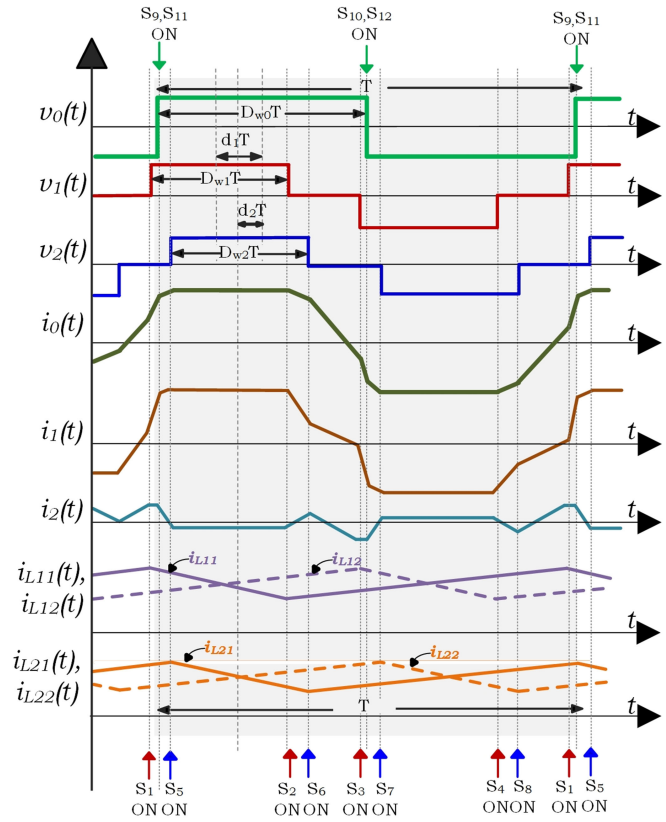

Fig. 2. Typical steady-state operating waveforms for the full bridge CF-TAB.

B. Operating Principle

In this TAB topology, when one pair of diagonal switches (S_1, S_4 for Port-1), (S_5, S_8 for Port-2), and (S_9, S_{12} for Port-0) are turned ON, positive voltage (equal to the respective clamp capacitor voltage) appears across the respective transformer windings. Similarly, when the other pair of diagonal switches conduct, the transformer voltage goes negative. The gate drive signals for the switches of the individual legs are complementary with respect to each other, and the two legs of each bridge are interleaved by 180°. Duty ratios of the input side bridges are determined in such a manner that the respective clamp capacitor voltages (v_{c1} & v_{c2} in Fig. 1) always remain constant irrespective of the battery and the FC voltage variations. The duty ratios of the load side bridge switches are fixed at 50%, to get maximum possible power transfer through the VF load side bridge. Fig. 2 shows typical waveforms of the transformer winding voltages, currents, and the filter inductor current for a fixed phase shift angle among the transformer voltages and the input side bridge duty ratios of 60%. The phase shift durations (d_1T, d_2T) are calculated, taking the load side voltage as the reference. In Fig. 2, interleaved filter inductor currents of the input bridges are shown individually, where the solid line and dotted line represents the leading and lagging leg filter inductor currents (i_{L11} and i_{L12} for battery port and i_{L21} and i_{L22} for FC port), respectively.

C. TAB Frequency Domain Modeling

A CF-TAB-based MPC, has five control variables namely the individual bridges duty ratios (d_0, d_B, d_F) and the phase

shift durations (d_1T, d_2T). These duty ratios can be varied between 0 and 1, whereas the phase shift durations are limited to $\pm 0.25T$, equivalent to $\pm 90^\circ$ phase shift. Leading phase shift angles are considered to be positive. A large number of control variables with a huge range of variation makes the determination of the operating modes very cumbersome. Therefore, in this article, the transformer voltage waveforms shown in Fig. 2 are decomposed into their equivalent secondary refereed Fourier series expressions as per (1)–(3)

$$v_0(t) = \sum_{n=1}^{\infty} (-1)^{n+1} \sqrt{2} V_{0n} \sin(2n-1)\pi w t \tag{1}$$

$$v_1'(t) = \sum_{n=1}^{\infty} (-1)^{n+1} \sqrt{2} V_{1n}' \sin((2n-1)\pi w t + \theta_{1n}) \tag{2}$$

$$v_2'(t) = \sum_{n=1}^{\infty} (-1)^{n+1} \sqrt{2} V_{2n}' \sin((2n-1)\pi w t + \theta_{2n}) \tag{3}$$

$$V_{1n}' = \frac{2\sqrt{2}V_{c1}'}{\pi} \frac{\sin(2n-1)\pi(D_{w1})}{2n-1} \tag{4}$$

$$V_{2n}' = \frac{2\sqrt{2}V_{c2}'}{\pi} \frac{\sin(2n-1)\pi(D_{w2})}{2n-1} \tag{5}$$

$$V_{0n} = \frac{2\sqrt{2}V_{c0}}{\pi} \frac{\sin(2n-1)\pi(D_{w0})}{2n-1} \tag{6}$$

where

$$\theta_{1n} = 2(2n-1)\pi d_1, \theta_{2n} = 2(2n-1)\pi d_2 \tag{7}$$

$$D_{wi}|_{(i=1,2,0)} = min(0.5, d_j, 1-dj)|_{(j=B,F,0)}. \tag{8}$$

In the above equations, V_{1n}' and V_{2n}', are the secondary referred rms values of the nth harmonic voltages of winding 1 and 2, respectively. V_{0n} is the rms value of the nth harmonic component of the secondary voltage. V_{c1}', V_{c2}' are the secondary referred clamp capacitor voltages for the primary bridges 1 and 2, respectively. D_{w1}, D_{w2}, and D_{w0} represents the pulse widths of the transformer winding voltages, respectively. θ_{1n} and θ_{2n} are the phase angles of the nth harmonic components of $v_1'(t)$ and $v_2'(t)$ with respect to the nth harmonic component of $v_0(t)$.

D. Steady-State Power Flow Equations

The secondary referred delta equivalent model of the three winding transformer [16], as shown in Fig. 3, is used to formulate the steady-state power flow equations. The output terminals of the three ports are modeled as independent voltage sources. P_1, P_2, P_0 are the total power coming out from the input Ports 1 and 2 and flowing into the output port, respectively. P_{10} represents the share of the power flow between winding 1 to the output port only. Similarly, P_{12}, P_{20} are the power flow between Port-1 to Port-2 and Port-2 to the load port, respectively. The overall power flow relation among P_1, P_2, P_0 is given by (9). These can further be represented in terms of voltage and phase shift angles as per (10)–(12), after summing the individual winding powers at each harmonic frequency. X_L represents the delta equivalent leakage inductance of the three winding transformer at the switching frequency. It is assumed to be the same for all

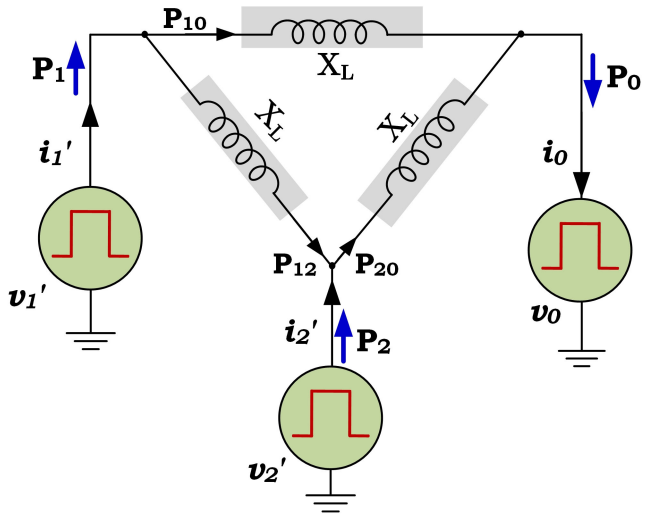

Fig. 3. Delta equivalent model of three winding transformer.

three windings

$$P_1 = P_{10} + P_{12}, P_2 = P_{20} - P_{12},$$
$$P_0 = P_{10} + P_{20}, P_1 + P_2 = P_0. \tag{9}$$

Therefore

$$P_1 = \sum_{n=1}^{\infty} \frac{V_{1n}' V_{0n} \sin(\theta_{1n})}{(2n-1)X_L} + \frac{V_{1_n}' V_{2_n}' \sin(\theta_{1n} - \theta_{2n})}{(2n-1)X_L} \tag{10}$$

$$P_2 = \sum_{n=1}^{\infty} \frac{V_{2n}' V_{0n} \sin(\theta_{2_n})}{(2n-1)X_L} + \frac{V_{1n}' V_{2n}' \sin(\theta_{2n} - \theta_{1n})}{(2n-1)X_L} \tag{11}$$

$$P_0 = \sum_{n=1}^{\infty} \frac{V_{1n}' V_{0n} \sin(\theta_{1_n})}{(2n-1)X_L} + \frac{V_{2_n}' V_{0_n} \sin(\theta_{2n})}{(2n-1)X_L}. \tag{12}$$

It is to be noted from (4)–(6) that each of the harmonic voltages (V_{1n}', V_{2n}', V_{0n}') in (9)–(12) are inversely proportional to $(2n-1)$. Therefore individual harmonic powers decreases as fast as $(2n-1)^3$. Hence, computing only first few terms of the "infinite sums" of the right-hand side (RHS) of (10) to (12) give accurate enough result for all practical purposes.

III. Closed-Loop Controller Design

A. State-Space Modeling

The proposed CF-TAB-based MPC is a nonlinear multiple input multiple output system. The state-space model of the system considering the switching cycle average Battery current (i_B), FC current (i_F), clamp capacitor voltages of three ports (v_{c1}, v_{c2}, v_{c0}) as the state variables can be written as (13)–(17). The states corresponding to the transformer leakage inductance currents are neglected (i.e., assumed to be algebric functions of the states and control inputs)

$$\frac{L_1}{2}\frac{di_B}{dt} = L_B \frac{di_B}{dt} = v_B - (1-d_B)v_{c1} \tag{13}$$

$$\frac{L_2}{2}\frac{di_F}{dt} = L_F \frac{di_F}{dt} = v_{\text{FC}} - (1-d_F)v_{c2} \tag{14}$$

$$C_1 v_{c1}\frac{dv_{c1}}{dt} = 2(1-d_B)v_{c1}i_{L1} - p_1 \tag{15}$$

$$C_2 v_{c2}\frac{dv_{c2}}{dt} = 2(1-d_F)v_{c2}i_{L2} - p_2 \tag{16}$$

$$C_0 v_{c0}\frac{dv_{c0}}{dt} = p_0 - \frac{v_{c0}^2}{R_0} \tag{17}$$

where

$$i_B = 2i_{L1}; i_F = 2i_{L2}; L_B = L_1/2, L_F = L_2/2. \tag{18}$$

In these equations, i_B, i_F are the total currents coming out from the battery and the FC, respectively, and i_{L1}, i_{L2} represents the switching cycle average value of individual inductor currents of Port-1 and Port-2, respectively. p_1, p_2, p_0 are the switching cycle averaged powers coming out of the two input ports and flowing into the output port, respectively, as per (10) to (12). The above state equations are next linearized around a quiescent value of the system state variables (i_B, i_F, v_{c1}, v_{c2}, v_{c0}), the control variables (d_B, d_F, d_1, d_2), as well as the input variables (v_B, v_{FC}). The switching cycle averaged powers (p_1, p_2, p_0) of each port are also linearized around a constant operating point by taking the Taylor series expansions of the power (10)–(12) and retaining only the dc and the linear terms as per

$$p_i|_{(i=1,2,0)} = P_i + \Delta p_i \tag{19}$$

where

$$\Delta p_i|_{(i=1,2,0)} = \frac{\partial p_i}{\partial d_B}\Delta d_B + \frac{\partial p_i}{\partial d_F}\Delta d_F + \frac{\partial p_i}{\partial d_1}\Delta d_1 + \frac{\partial p_i}{\partial d_2}\Delta d_2 + \sum_{j=0}^{2}\frac{\partial p_i}{\partial v_{cj}}\Delta v_{cj}. \tag{20}$$

The quiescent values can be obtained for a given operating condition by solving the algebric equations obtained by setting the derivative terms in (13)–(17) to zero. Similarly, the quiescent input and output power (P_1, P_2, P_0) can be calculated from (10)–(12). Considering only the small signal perturbations of the states and the input variables (indicated by a "Δ" preceding the variable name) and neglecting the dc and nonlinear terms, the small signal model equations for the MPC can be formulated as given in

$$\frac{L_1}{2}\frac{d\Delta i_B}{dt} = \Delta v_B - (1-D_B)\Delta v_{c1} + V_{c1}\Delta d_B \tag{21}$$

$$\frac{L_2}{2}\frac{d\Delta i_F}{dt} = \Delta v_{\text{FC}} - (1-D_F)\Delta v_{c2} + V_{c2}\Delta d_F \tag{22}$$

$$C_1\frac{d\Delta v_{c1}}{dt} = (1-D_B)\Delta i_B - \Delta d_B I_B - \Delta i_{c1} \tag{23}$$

$$C_2\frac{d\Delta v_{c2}}{dt} = (1-D_F)\Delta i_F - \Delta d_F I_F - \Delta i_{c2} \tag{24}$$

$$C_0\frac{d\Delta v_{c0}}{dt} = \Delta i_{c0} - \frac{\Delta v_{c0}}{R_0} \quad \text{where, } \Delta i_{ci}|_{i=1,2,0} = \Delta p_i/V_{ci}. \tag{25}$$

For the proposed MPC, there are three main control objectives as follows:

1) constant current control for the FC;
2) load side dc bus voltage control under all possible operating condition;
3) transformer voltage matching with input bridges duty ratio control;

In view of the above control requirements, the FC current and the load side dc bus voltage are considered as the output variables that need to be controlled. The duty ratios of the CF input bridges and the two phase shift durations forms the control input vector, while the battery and FC input voltages form the disturbance input vector. Now, the small signal state-space representation of the proposed MPC considering the abovementioned control requirement can be written as per (26) and (27), respectively

$$\Delta\dot{X} = A\Delta X + B\Delta U_C + E\Delta U_D \tag{26}$$

$$\Delta Y = C\Delta X + D\Delta U_C + F\Delta U_D \tag{27}$$

where

$$\Delta X = \begin{bmatrix}\Delta i_B & \Delta i_F & \Delta v_{c1} & \Delta v_{c2} & \Delta v_{c0}\end{bmatrix}^T \tag{28}$$

$$\Delta Y = \begin{bmatrix}\Delta i_F & \Delta v_{c0}\end{bmatrix}^T \tag{29}$$

$$\Delta U_C = \begin{bmatrix}\Delta d_B & \Delta d_F & \Delta d_1 & \Delta d_2\end{bmatrix}^T$$

$$\Delta U_D = \begin{bmatrix}\Delta v_B & \Delta v_{\text{FC}}\end{bmatrix}^T. \tag{30}$$

$\Delta X, \Delta Y, \Delta U_C, \Delta U_D$ represent the state vectors, output vector, control vector, and disturbance input vector, respectively. Perturbation due to the source voltages are neglected. A, B, C, D are system matrices whose elements can be found from (21)–(25). The above system model has been used further to design two different system controllers.

B. Design of the State Feedback Controller

The overall state feedback control scheme for the MPC converter is presented in Fig. 4. Taking the transformer secondary side voltage as the reference, the PWM signals for the input bridges are generated with variable phase shift durations d_1 and d_2. As the FC and the battery voltages vary slowly, the duty ratio (d_B and d_F) variations are considered to be slow compared to the phase shift control loop. Therefore, these are computed in open-loop manner (to keep the respective clamp capacitor voltages constant) to reduce control complexity. As Δd_B and Δd_F are utilized to neutralize the input disturbances Δv_B and Δv_{FC} respectively in open loop manner, the control input vector consists of only the phase shift durations (d_1 and d_2) as the feedback control variables. Further, along with the system states presented in (28), two more state variables (ΔX_1 and ΔX_2) are added to the state vector as shown in (31) to fulfill the control objectives. Those are the integrator outputs of the load voltage and FC current error, respectively, as shown in (33). In this equation, I_F^*, V_{c0}^* are the reference values for the

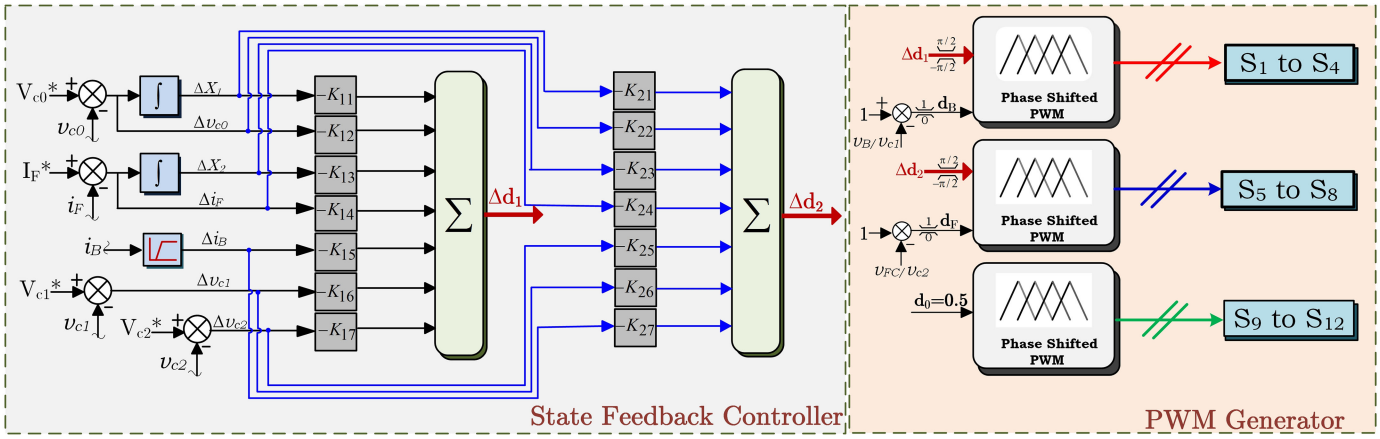

Fig. 4. Overall control structure for state feedback control.

FC current and the load voltage.

$$\Delta X = \begin{bmatrix} \Delta X_1 & \Delta X_2 & \Delta i_B & \Delta i_F & \Delta v_{c1} & \Delta v_{c2} & \Delta v_{c0} \end{bmatrix}^T \tag{31}$$

$$\Delta Y = \begin{bmatrix} \Delta i_F & \Delta v_{c0} \end{bmatrix}^T ; \Delta U_C = \begin{bmatrix} \Delta d_1 & \Delta d_2 \end{bmatrix}^T \tag{32}$$

$$p\Delta\dot{X}1 = \Delta i_F = (I_F^* - i_F); \quad p\Delta\dot{X}2 = \Delta v_{c0} = (V_{c0}^* - v_{c0}). \tag{33}$$

The control vector ΔU_C is computed in the following state feedback form as per the below equation:

$$\Delta U_C = -K\Delta X \tag{34}$$

$$K = \begin{bmatrix} K_{11} & K_{12} & K_{13} & K_{14} & K_{15} & K_{16} & K_{17} \\ K_{21} & K_{22} & K_{23} & K_{24} & K_{25} & K_{26} & K_{27} \end{bmatrix} \tag{35}$$

where *K* is the gain matrix, whose elements are calculated using Ackermen's Gain formula and the system matrix A. The gain matrix is designed in such a way that the roots of the closed-loop characteristic equation are located at the desired pole locations. For the proposed MPC, the closed-loop pole locations are chosen in a Butterworth pattern, as detailed later in Section IV.

C. Decoupled Proportional Integral Controller Design

The power transfer across the transformer windings from the individual ports are functions of both the phase shift angles. Therefore, a decoupled controller is proposed to regulate the dc bus voltage and the FC current.

1) Small Signal AC Equivalent Circuit Model: An equivalent circuit model for the proposed MPC can be drawn as shown in Fig. 5 using (19)–(25). As both the input CF ports are identical, both of them can be modeled in a similar manner. Therefore, modeling of only Port-1 is described in detail here. The small signal equivalent circuit of the input Port-1 is formulated as per Fig. 5(a). The inductor (21) is modeled as voltages around a loop containing an inductor, while the capacitor (23) is modeled as currents flowing into/out of a node containing a capacitor. These two subsystems are coupled by a $(1-D_B{:}1)$ ideal transformer representing the action of the boost converter. The final small signal ac equivalent circuit for Port-1 as shown in Fig. 5(b) is obtained by referring the left hand side (LHS) of this ideal transformer to the RHS using "turns ratio" $(1-D_B)$. Further, the secondary refereed equivalent circuit model for the load side converter is formulated as per Fig. 5(c) from (25). In these equivalent circuits, Δd_B, Δd_F are computed as per

$$\Delta d_B = -\frac{\Delta v_B}{V_{C1}}, \Delta d_F = -\frac{\Delta v_{\mathrm{FC}}}{V_{C2}}. \tag{36}$$

With this equation, the model of the input CF ports can be simplified to the first two circuits of Fig. 5(d). In these circuits Δi_{dc1}, Δi_{dc2} represents the sums of all the dependent current sources connected to the capacitor node. Similarly, the secondary referred equivalent circuit model for the Port-0 shown in Fig. 5(c) can be further simplified to the last circuit of Fig. 5(d). From the small signal models of the individual bridges, Δi_{dc1}, Δi_{dc2} and Δi_{dc0} can be written as per

$$\begin{bmatrix} \Delta i_{dc1} \\ \Delta i_{dc2} \\ \Delta i_{dc0} \end{bmatrix} = A_1 \begin{bmatrix} \Delta d_1 \\ \Delta d_2 \\ \Delta d_B \\ \Delta d_F \end{bmatrix} + B_1 \begin{bmatrix} \Delta v_{c1} \\ \Delta v_{c2} \\ \Delta v_{c0} \end{bmatrix} \tag{37}$$

$$A_1 = \begin{bmatrix} \frac{\partial i_{c1}}{\partial d_1} & \frac{\partial i_{c1}}{\partial d_2} & I_B + \frac{\partial i_{c1}}{\partial d_B} & \frac{\partial i_{c1}}{\partial d_F} \\ \frac{\partial i_{c2}}{\partial d_1} & \frac{\partial i_{c2}}{\partial d_2} & \frac{\partial i_{c2}}{\partial d_B} & I_F + \frac{\partial i_{c2}}{\partial d_F} \\ \frac{\partial i_{c0}}{\partial d_1} & \frac{\partial i_{dc0}}{\partial d_2} & \frac{\partial i_{c0}}{\partial d_B} & \frac{\partial i_{c0}}{\partial d_F} \end{bmatrix} \tag{38}$$

$$B_1 = \begin{bmatrix} \frac{\partial i_{c1}}{\partial v_{c1}} & \frac{\partial i_{c1}}{\partial v_{c2}} & \frac{\partial i_{c1}}{\partial v_{c0}} \\ \frac{\partial i_{c2}}{\partial v_{c1}} & \frac{\partial i_{c2}}{\partial v_{c2}} & \frac{\partial i_{c2}}{\partial v_{c0}} \\ \frac{\partial i_{c0}}{\partial v_{c1}} & \frac{\partial i_{c0}}{\partial v_{c2}} & \frac{\partial i_{c0}}{\partial v_{c0}} \end{bmatrix}. \tag{39}$$

As the Battery and FC voltages vary very slowly in a small range, the dynamics of the control variables due to Δd_B, Δd_F are neglected for the phase shift controller (Δd_1, Δd_2) design. Δd_B, Δd_F are directly chosen as per (36). To design the phase shift controller a new control vector $\Delta X = [\Delta X_1\ \Delta X_2\ \Delta X_0]$

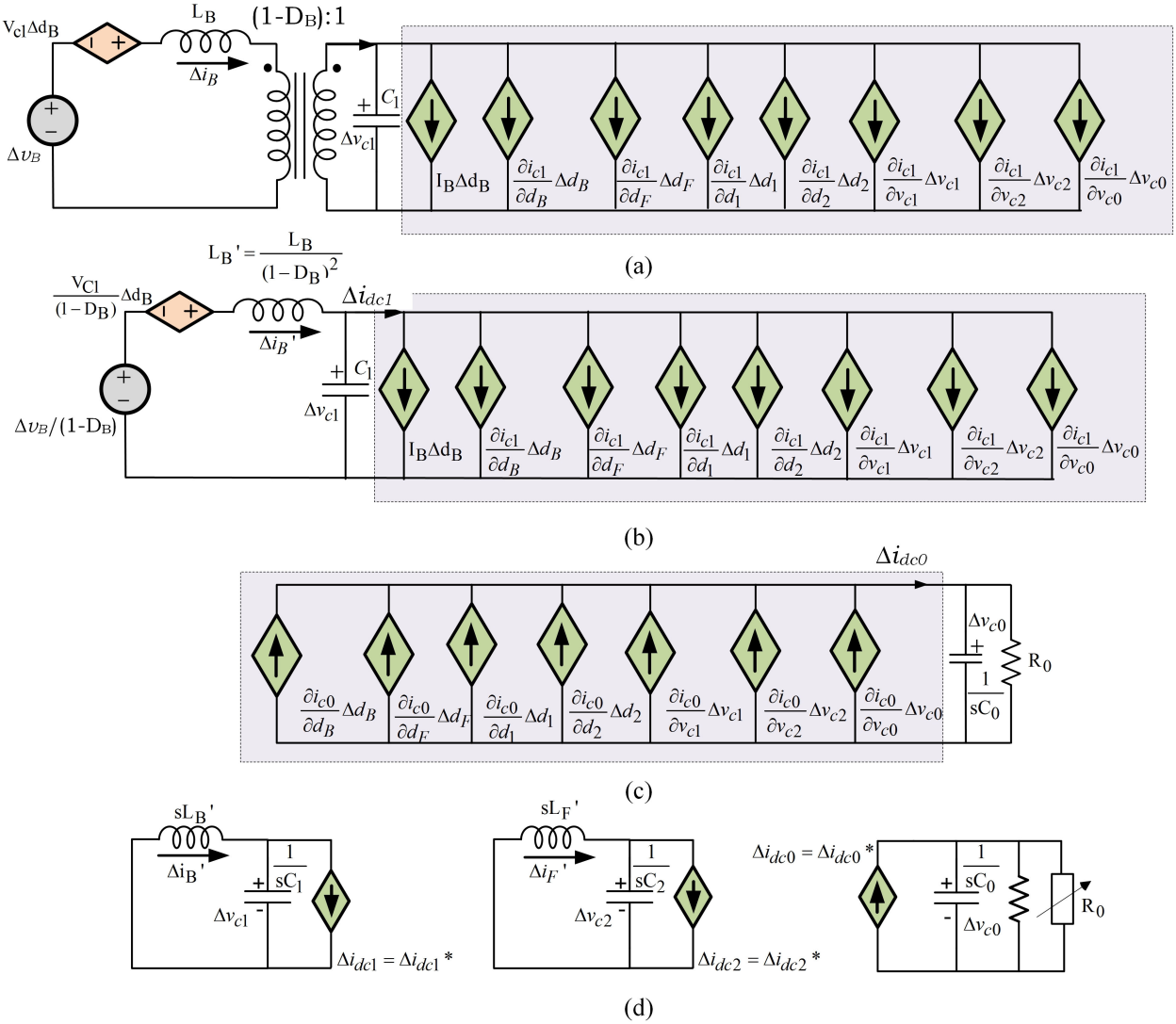

Fig. 5. Small signal average equivalent model for (a) Port-1, (b) Port-1 (secondary referred), (c) Port-0 (d) Final small signal equivalent model for all three ports.

is defined as per the following:.

$$\begin{bmatrix}\Delta X_1\\ \Delta X_2\\ \Delta X_0\end{bmatrix} = \begin{bmatrix}\frac{\partial i_{c1}}{\partial d_1} & \frac{\partial i_{c1}}{\partial d_2}\\ \frac{\partial i_{c2}}{\partial d_1} & \frac{\partial i_{c2}}{\partial d_2}\\ \frac{\partial i_{c0}}{\partial d_1} & \frac{\partial i_{c0}}{\partial d_2}\end{bmatrix}\begin{bmatrix}\Delta d_1\\ \Delta d_2\end{bmatrix}. \tag{40}$$

If the output current references (at the clamp capacitor nodes) of the two input bridges and the input current reference (at the dc bus capacitor node) are defined as

$$\begin{aligned}\Delta i^*_{\rm dc1} &= \frac{\partial i_{c1}}{\partial v_{c1}}\Delta v_{c1} + \frac{\partial i_{c1}}{\partial v_{c2}}\Delta v_{c2} + \frac{\partial i_{c1}}{\partial v_{c0}}\Delta v_{c0} + \Delta X_1\\ \Delta i^*_{\rm dc2} &= \frac{\partial i_{c2}}{\partial v_{c1}}\Delta v_{c1} + \frac{\partial i_{c2}}{\partial v_{c2}}\Delta v_{c2} + \frac{\partial i_{c2}}{\partial v_{c0}}\Delta v_{c0} + \Delta X_2\\ \Delta i^*_{\rm dc0} &= \frac{\partial i_{c0}}{\partial v_{c1}}\Delta v_{c1} + \frac{\partial i_{c0}}{\partial v_{c2}}\Delta v_{c2} + \frac{\partial i_{c0}}{\partial v_{c0}}\Delta v_{c0} + \Delta X_0\end{aligned} \tag{41}$$

then on combining (41) with (40) and comparing with, (37)–(39) results in $\Delta i_{\rm dc1} = \Delta i^*_{\rm dc1}$, $\Delta i_{\rm dc2} = \Delta i^*_{\rm dc2}$, $\Delta i_{\rm dc0} = \Delta i^*_{\rm dc0}$, as indicated in Fig. 5(c). Therefore, the capacitor voltages and the inductor currents in the equivalent circuits of Fig. 5(d) (i.e., Δv_{c1}, Δv_{c2}, Δv_{c0}, $\Delta i'_B$ and $\Delta i'_F$) can be controlled by controlling the controllable current sources $\Delta i^*_{\rm dc1}$, $\Delta i^*_{\rm dc2}$ and $\Delta i^*_{\rm dc0}$. The desired values of these current references are then used in (41) to obtain the values of the control inputs ΔX_1, ΔX_2, ΔX_0. However, the variables ΔX_1, ΔX_2, ΔX_0 are linearly dependent and all are functions of Δd_1, Δd_2. Thus, any two of them can be controlled independently. This will automatically determine the third. The objective of the present controller is to control the load voltage and the FC output current. Keeping that in mind, $\Delta d_1, \Delta d_2$ are computed as functions of ΔX_0 and ΔX_2 as per (42), since $\Delta i^*_{\rm dc0}$ and $\Delta i^*_{\rm dc2}$ directly controls the load voltage and the FC current, respectively

$$\begin{bmatrix}\Delta d_1\\ \Delta d_2\end{bmatrix} = \begin{bmatrix}\frac{\partial i_{c2}}{\partial d_1} & \frac{\partial i_{c2}}{\partial d_2}\\ \frac{\partial i_{c0}}{\partial d_1} & \frac{\partial i_{c0}}{\partial d_2}\end{bmatrix}^{-1}\begin{bmatrix}\Delta X_2\\ \Delta X_0\end{bmatrix} = \begin{bmatrix}a_{11} & a_{12}\\ a_{21} & a_{22}\end{bmatrix}\begin{bmatrix}\Delta X_2\\ \Delta X_0\end{bmatrix}. \tag{42}$$

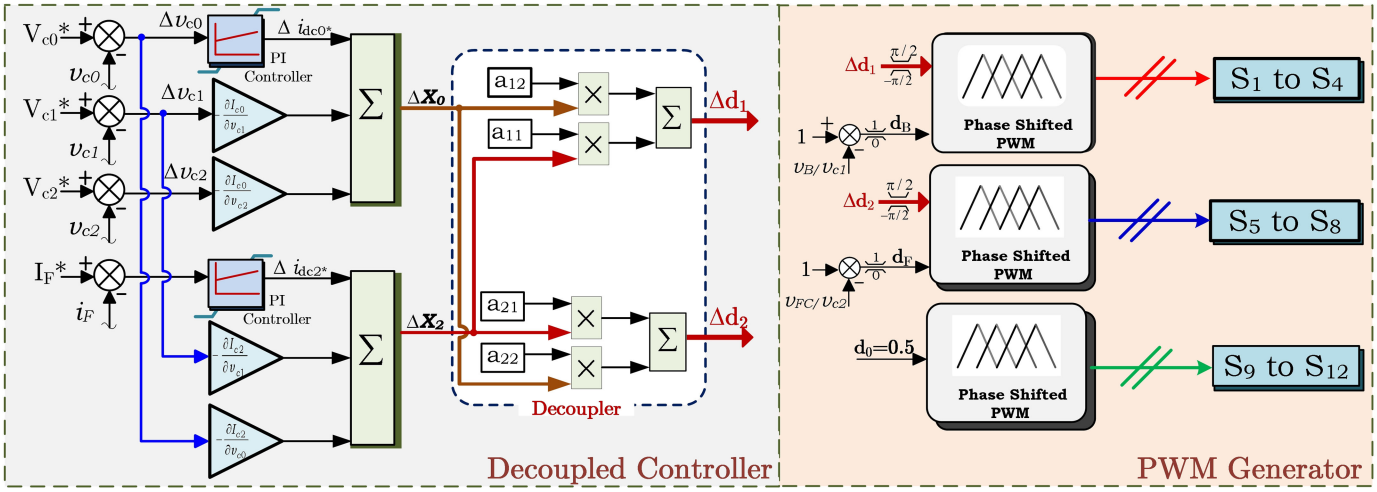

Fig. 6. Overall closed-loop control structure for PI-based decoupled control.

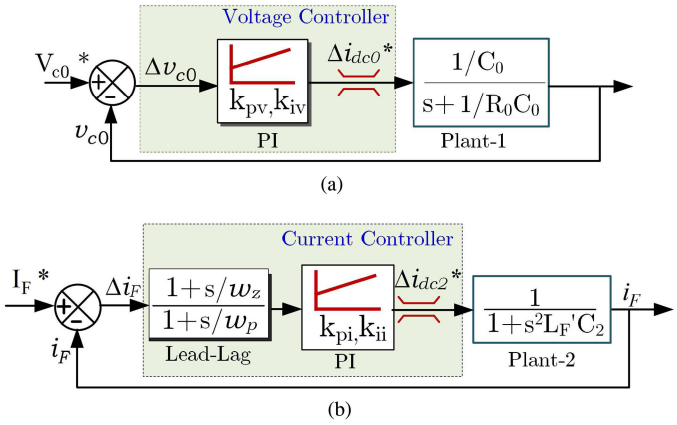

Fig. 7. Individual closed loop controllers for (a) Load side dc bus voltage control. (b) Constant current control.

From the above analysis, the overall control strategy for the small-signal equivalent circuit based approach can be formulated as per Fig. 6. As per this figure, $\Delta i^*_{\mathrm{dc0}}$ and $\Delta^* i_{\mathrm{dc2}}$ are generated from the load voltage and the FC current PI controllers, respectively, and are used to generate ΔX_0, ΔX_2 as per (41). Finally, the perturbation in the phase shift durations (Δd_1, Δd_2) are generated as per (42) and added with the nominal phase shift durations D_1, D_2 to generate the actual phase shifts. The duty ratios of the input bridges, along with the phase shift angles are given as the inputs to the PWM block to generate actual switching signals for the individual switches.

2) Design of Controllers for the Load Voltage and FC Current Control Loops: To design the PI controllers for the load voltage and the FC current, the uncompensated system plant models are formulated as per Fig. 7(a) and (b) (Plant-1 for load voltage control and Plant-2 for FC current control), respectively, from the last two equivalent circuits of Fig. 5(d). As the plant model for the load voltage controller is first order only, a PI controller is enough to get the desired bandwidth and phase margin. The values of the PI controller gains are decided accordingly. On the other hand, a lead-lag compensator along with a PI controller is designed for the FC current control loop as this plant has a pair of imaginary poles. In this case, the pole-zero locations of the lead-lag compensator, along with the PI controller gains, are chosen in such a way that the current control loop becomes faster compared to the load voltage control loop. Actual designed values of the controller parameters are given in Table I.

TABLE I
PARAMETERS FOR PI-BASED DECOUPLED CONTROLLER

Voltage Controller			
k_{pv}	k_{iv}	Bandwidth	Phase Margin
0.001	35	80 Hz	90°
Current Controller			
k_{pi},k_{ii}	f_z, f_p(kHz)	Bandwidth	Phase Margin
4,100	0.296, 3.5	100 Hz	52.2°

3) Stability Analysis With Operating Point Variation: In the proposed MPC, two separate PI controllers have been designed for the load voltage control, and the FC current control. The system parameters used for the study are presented in Table II. The PI controller parameters are designed based on the transfer functions of the individual loops presented in Fig. 7, computed at the operating point. $v_B = 57$ V, $v_{\mathrm{FC}} = 30$ V, $P_1 = 500$ W, $P_2 = 500$ W, $P_0 = 1000$ W. The decoupling matrix is also designed at the same operating point. The values of PI controller gains used for the proposed decoupled controller is presented in Table I. Now, the closed loop pole locations will vary, with the variation of source voltages (v_B, v_{FC}), as well as the power values (P_0, P_1, P_2), since the individual controller gains and the decoupling matrix parameters are kept fixed at their respective designed values. In fact a fixed decoupling matrix will not be effective at other off nominal operating points. Therefore, the closed loop block diagrams of Fig. 7 will not give correct closed loop pole locations at an off nominal operating point. So, to get the exact closed loop pole locations, an augmented system matrix is formulated incorporating the states related to individual

TABLE II
SYSTEM AND TRANSFORMER SPECIFICATIONS

System Specifications			
Parameters	**Values**	**Parameters**	**Values**
V_B	$48-56\,V$	V_{FC}	$20-30\,V$
P_1,P_2	$0-500\,W$	P_0	$0-1\,kW$
V_{c1}/V_{c2}	$110\,V/55\,V$	V_{c0}	$220\,V$
f_s	25 kHz	L_1, L_2	$150\,\mu$H
L_{l1}, L_{l2}	$38.27\,\mu$H, $9.7\,\mu$H	L_{l0}	$155.28\,\mu$H
Transformer Specifications			
Parameters	**Values**	**Parameters**	**Values**
$V_1:V_2:V_0$	2: 1: 4	L_m	17 mH
Core Type	E-100/60/28/3C-94	Window Area	$7.32\,cm^2$
Core Area	$7.38\,cm^2$	Peak flux density	$0.12\,T$
Core loss coefficient	$3.14\text{W}/m^3T^\beta$	Current density	$4\,A/mm^2$

β=core loss exponent=2.551 at f_s

PI controllers and the decoupling matrix parameters. The eigen values of this augmented system matrix gives the closed loop pole location of the overall system. These eigen values are plotted for three different system operating conditions. It is to be noted that while calculating the eigen values of the augmented system at different system operating equations the PI controller and the decoupling matrix parameters are kept fixed at their respective nominal designed values. Fig. 8(a) shows the location of closed loop poles when the battery voltage varies from 48 to 57 V, while v_{FC} is kept fixed at 29 V, load power P_0 is kept at its rated value of 1000 W with the battery and the FC powers are considered to remain fixed at 400 and 600 W, respectively. Similar study has been performed for the same power values, but with the FC voltage (v_{FC}) varying from 22 to 29 V, keeping battery voltage constant at 54 V. In both the cases, all the closed loop poles lies in the left half of the s plane [Fig. 8(a) and (b)], which confirms system stability. The poles on the real axis vary within a very small range with the operating point variation. Fig. 8(c) shows the location of the closed loop poles for the load power variation with fixed V_B and v_{FC} of 57 and 29 V, respectively. In this case, as the load power changes, the power sharing among the sources has to change. Thus, the three operating points related to power are chosen as ($P_0 = 1000$ W, $P_1 = 500$ W, $P_2 = 500$ W), (P_0=600 W, $P_1 = 360$ W, $P_2 = 240$ W), ($P_0 = 1000$ W, $P_1 = 280$ W, $P_2 = 120$ W), respectively. As can be seen from Fig. 8(c), almost all the closed loop poles remain within a very close range with the load power variation. It has been seen that, if the sharing among the P_1 and P_2 changes for a fixed P_0, v_B, and v_{FC}, the similar phenomenon takes place. It is to be noted that the range of variation of different system variables (i.e., v_B and v_{FC}, P_0, P_1, P_2) were chosen as per the designed range of variation of these variables as given in Table II.

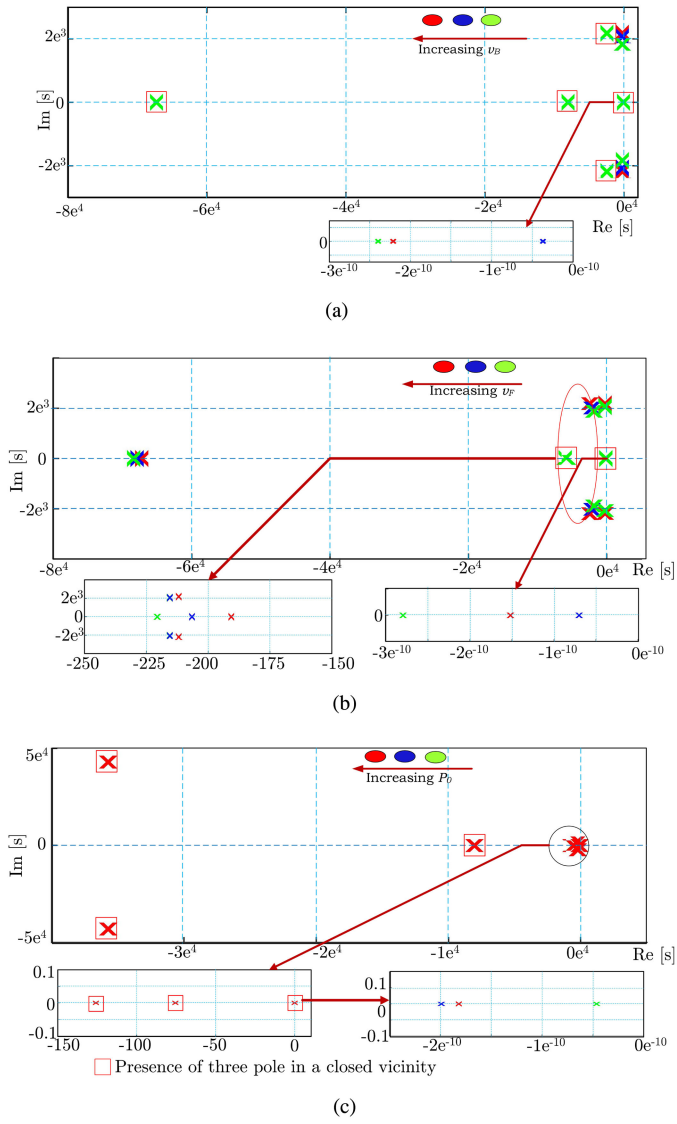

Fig. 8. Closed loop pole location of the overall system for (a) the variation of battery voltage (v_B) with v_{FC}, P_0, P_1, P_2 fixed (b) the variation of FC voltage (v_{FC}) with v_B, P_0, P_1, P_2 fixed (c) the variation of load power with v_B, v_{FC} fixed.

IV. SIMULATION RESULTS AND COMPARATIVE STUDY

The proposed MPC with both the controllers (i.e., Figs. 4 and 6) are simulated for identical system conditions and load changes. The system parameters used for simulation study are presented in Table II. A step changing load pattern is considered to validate the dynamic performance of the proposed controllers.

For the state feedback controller, the closed-loop pole locations (P_1 to P_7) are chosen as per Table III. One real pole and six complex poles are chosen in Butterworth pattern with three different natural frequencies. The location of the dominant pole

TABLE III
PARAMETERS FOR THE STATE FEEDBACK CONTROLLER

P_1	P_2	P_3	P_4	P_5	P_6	P_7
-1500	$-100+70j$	$-100-70j$	$-400+280j$	$-400-280j$	$-700+420j$	$-700-420j$
K_{11}	K_{12}	K_{13}	K_{14}	K_{15}	K_{16}	K_{17}
-8.4959	17.0538	0.12	0.027	-0.0261	-0.0057	0.1534
K_{21}	K_{22}	K_{23}	K_{24}	K_{25}	K_{26}	K_{27}
-0.8809	15.467	0.0957	0.0367	-0.0169	-0.0221	0.1290

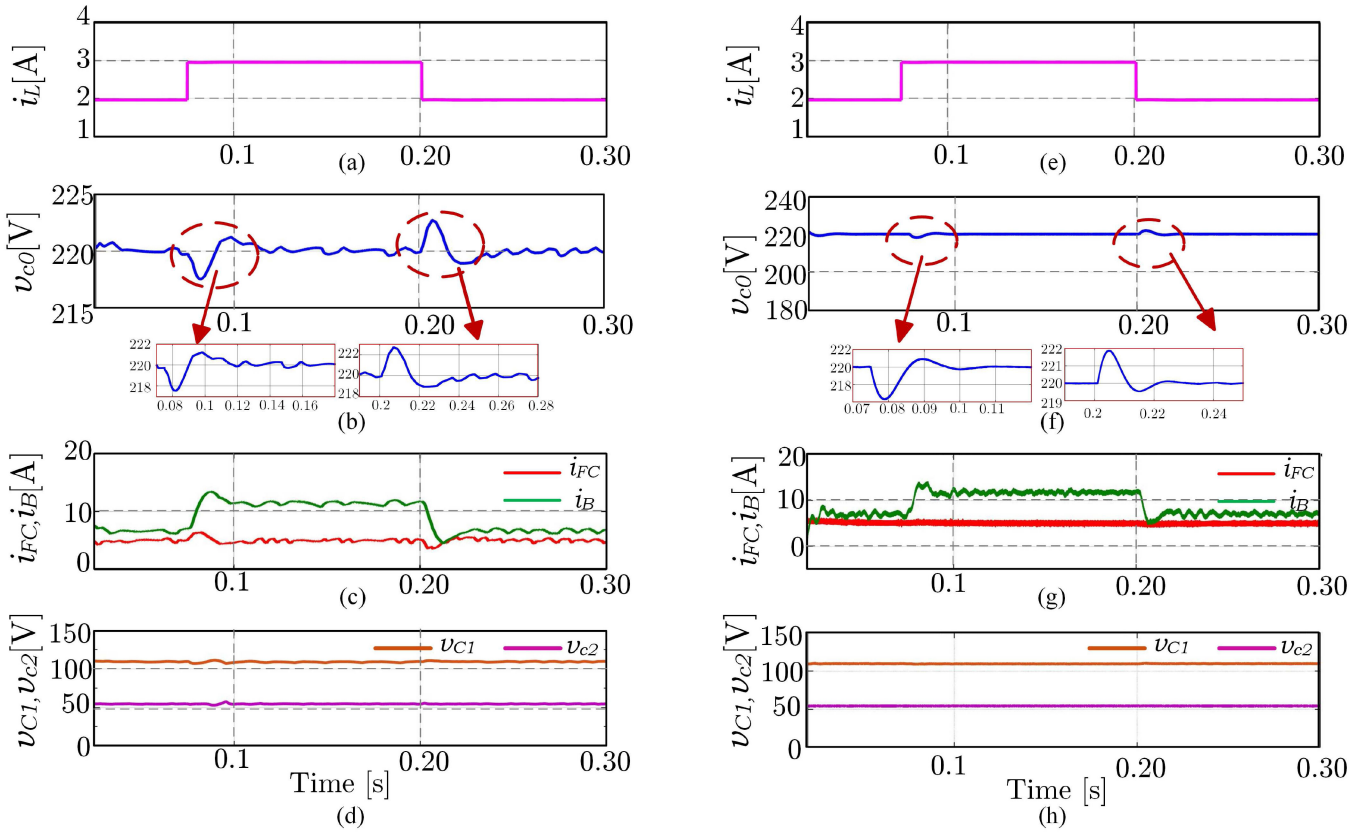

Fig. 9. Simulation waveforms to verify the state feedback controller performance during dynamic condition (a) load current profile (i_L), (b) variation of the load side dc bus voltage (v_{c0}) (c) FC and battery current ($i_{\rm FC}$, i_B), (d) input side dc bus voltage (v_{c1}, v_{c2}), PI-based decoupled controller performance during dynamic condition (e) load current profile (i_L), (f) variation of load side dc bus voltage (v_{c0}) (g) FC and battery current ($i_{\rm FC}$, i_B), (h) input side dc bus voltage (v_{c1}, v_{c2}).

is chosen to achieve the desired bandwidth and overshoot for the rated operating condition. The other frequencies are chosen within the reachable and observable Eigen values of the system matrix "A." One real pole is chosen at a sufficiently higher frequency so that it does not affect the dominant pole response. While choosing the complex pole locations, the damping factor for all the pairs are maintained greater than 0.7 to achieve overshoot less than 5%. After choosing the desired pole locations, the gain matrix "K" is calculated using Ackermen's gain calculation formula. The calculated gain values of the *K* matrix elements are also shown in Table III. Fig. 9(a)–(d) shows the performance of the state feedback control system, during a step load current change. The load current is changed from 2 to 3 A as shown in Fig. 9(a). Fig. 9(b) shows that in spite of the sudden change in the load current/power, load side dc bus voltage is maintained constant at 220 V dc. A voltage undershoot of -1% with settling time of around 70 ms occurs when the load changes from 440 to 660 W at 0.07 s. Similarly, a overshoot of +0.977% with settling time of 55 ms is observed at 0.2 s when the load decreases again from 660 to 440 W. The FC is controlled at a constant current of 5 A corresponding to 120 W output throughout the period. Thus, the battery power changes with the change in load, to absorb/supply the excess/deficit power demand in order to maintain fixed load voltage. This can be verified from the battery and the FC current waveforms presented in Fig. 9(c). The duty ratios of the input side bridges are regulated in such a way that the input dc bus voltages are fixed at 110 and 55 V, respectively. This can be verified from the input dc bus voltage waveforms of the battery and the FC port presented in Fig. 9(d).

Further, the system performance is verified by simulating the PI-based decoupled control system of Fig. 6. The values of the PI controller gains used for the proposed decoupled controller is presented in Table I. The same load profile [Fig. 9(e)] and operating conditions that have been used for the state feedback

controller is used to verify the performance of the proposed control strategy. It can be seen that, with the PI controller also the dc bus voltage is maintained constant at 220 V as per Fig. 9(f). But the undershoot and the overshoot in the load side dc bus voltage are negligible (-0.81% and $+0.86\%$, respectively) with an improved settling time of 50 ms, compared to the state feedback-based control technique. The FC current is regulated at a constant value throughout [Fig. 9(g)]. However, the battery current, in this case, is more oscillatory, since it is not directly controlled. Fig. 9(h) confirms that the input dc bus voltages are still maintained at their respective reference values of 110 and 55 V. The controller response with state feedback control is closely related to the system pole locations. Unfortunately, there is no unambiguous guideline for choosing these pole locations from conventional control system performance specifications (i.e., bandwidth, overshoot, settling time, etc.), particularly for higher order systems. It is also hard to customize the performance of the individual controllers (in this case load voltage and FC current controller) separately. On the other hand, the PI-based decoupled power controller design technique defines individual controller bandwidth and phase margins with less design complexity. The simulation results verify that the decoupled PI-based controller gives better response time (50 ms) for a 22% load change, compared to the state feedback control response time (70 ms). The proposed decouple control also reduces the voltage overshoot and undershoot to 0.86% from 1%. However, finding the appropriate decoupling strategy [i.e. (42)] may be difficult, if higher number of control variables are involved.

V. Experimental Results

To validate the proposed controller design approaches, a 1-kW laboratory prototype of the MPC has been developed as shown in Fig. 10. The parameters considered for the laboratory prototype and transformer design are given in Table II, where L_{l1}, L_{l2}, L_{l0}, L_m represents total effective leakage inductance (external+transformer leakage inductance) and magnetizing inductance of the transformer. The transformer leakage inductance, input side clamp capacitor voltages, and the transformer turns ratios have been calculated in order to get the rated power transfer capability with minimum transformer rms current. The detailed design methodology has been presented in detail in [23]. A moderate value for the input filter inductors (150 μH) has been chosen in order to get full range ZVS without increasing the input inductor rms currents excessively [23]. With the chosen values of the filter inductors, the peak to peak ripple in the battery and the FC port filter inductor currents are $\pm 13.5\%$ and $\pm 6.75\%$, respectively. But due to the ripple cancellation effect, the source current ripple gets further reduced. For the battery and the FC side bridges:STW78N65M5 MOSFET (650 V, 69 A) and for the load side switches:SKM75GB12T4 IGBTs (1.2 kV) are chosen. The output capacitance (C_{0ss}) for the MOSFET is 158 pF and for the IGBTs, it is 200 pF. The dead time among the complementary switches of each port are chosen such that, during turning ON/OFF of the respective switches the switch output capacitance get enough time to discharge and charge, respectively. The dead time for the input side bridges and the load side bridges have been chosen as 600 ns and 1 μs, respectively.

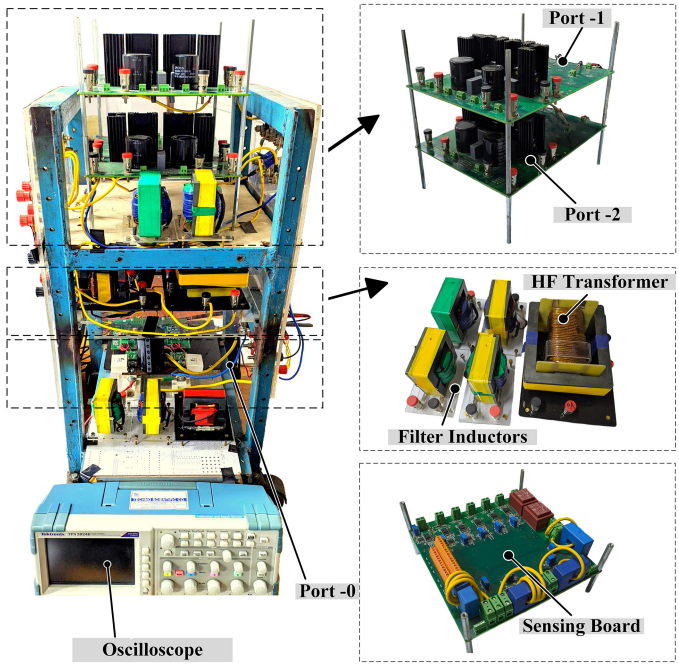

Fig. 10. Laboratory experimental setup of the MPC converter.

The experimental results have been taken at the rated operating voltages. Fig. 11(a)–(c) shows the steady-state experimental waveforms of all three transformer voltages with (a) primary winding-1, (b) primary winding-2, and (c) secondary winding currents, respectively. In this case, the load power P_0 is maintained at 420 W, whereas the battery and the FC voltages are kept at 44.2 and 22.85 V, respectively. The duty ratio d_B, d_F for the bottom switches of the battery and FC ports are 0.6, in order to regulate input side dc bus voltages at 112 and 55.5 V, respectively. The phase shift angles are kept such that the FC supplies a constant power of 167 W and the rest of the power is supplied by the Battery to maintain the load side dc bus voltage at 220 V. The FC is supplying a constant current of 7.3 A and the battery is also discharging at a current of 6.55 A in order to supply the deficit load demand as shown in Fig. 12(a) and (b). The input filter current waveforms of the two input side bridges presented in these figures confirm that the individual inductor current ripples are in phase opposition with each other, which effectively smoothen out the source current ripple.

Another set of steady-state operating waveforms are also presented to show the battery charging operation. To do that, the system is operated at a very light load condition of 90 W only. The FC is forced to supply a constant 310 W power, a part of which is utilized for the battery charging. Fig. 13(a) shows the battery charging operation with negative total battery current and individual filter inductor currents for the battery port. Fig. 13(b) shows the primary voltages and currents of the transformer winding, where it can be found that the battery port (primary winding-1) voltage is lagging behind the FC port voltage (primary winding-2), which again confirms that the battery is charging, from excess FC power.

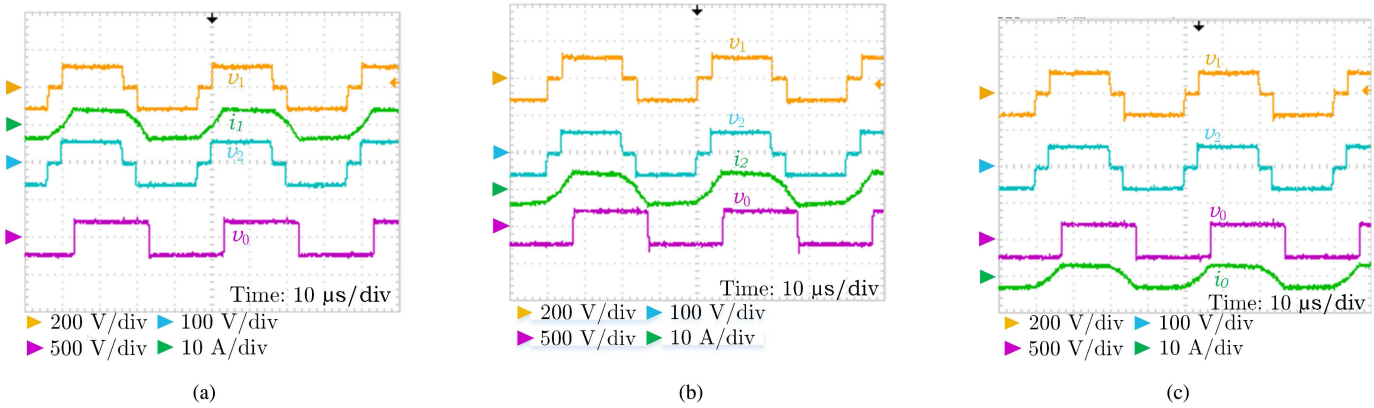

Fig. 11. Steady-state operating waveforms for $P_0 = 420$ W, $V_B = 44.2$ V, $V_{FC} = 22.85$ V. Transformer voltages with (a) Primary winding-1 leakage inductor current i_1. (b) Primary winding-2 leakage inductor current i_2. (c) Secondary winding leakage inductor current i_0.

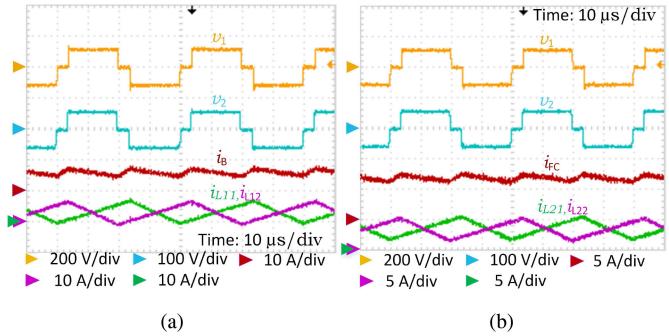

Fig. 12. Steady-state current waveforms for $P_0 = 420$ W,$I_B = 6.55$ A, $I_{FC} = 7.3$ A. (a) Battery port (Port-1) individual input filter inductor current i_{L1}. (b) FC port (Port-2) individual input filter inductor current i_{L2}.

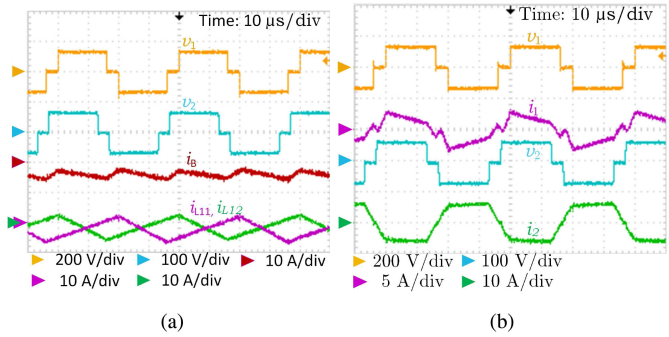

Fig. 13. Steady-state operating waveforms during reverse power flow (Battery charging), for $P_0 = 90$ W, $I_B = -3.1$ A, $I_{FC} = 10.8$ A. (a) Individual filter inductor and overall battery charging current (i_B). (b) Port-1, Port-2 transformer primary winding voltages and currents.

Experimental verification of the proposed PI-based decoupled control system is taken up next. The system is tested for a step change in the load, where the initial load power of 198 W is increased in one step to 440 W and again decreased back to 198 W. It can be seen from Fig. 14(a), that in spite of the application of a step change in the load the dc bus voltage is maintained at its reference value of 220 V. The FC current is also controlled at constant 5 A corresponding to an FC power

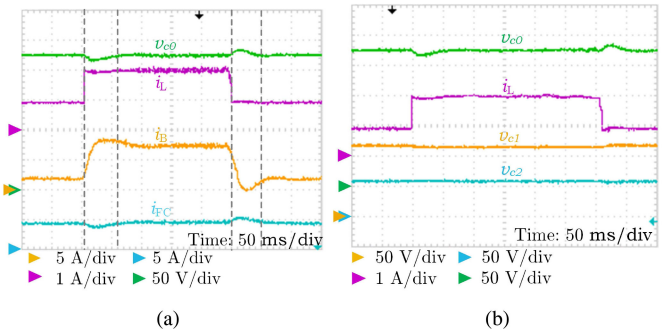

Fig. 14. Closed-loop performance of the proposed PI-based decoupled controller for load transient. (a) Transient response for step load increase of 198 to 440 W and back with constant FC power of 120 W. (b) Waveforms of input clamp capacitor voltages during load change.

of 120 W. The FC voltage was at 24 V, while the battery voltage was at 41 V. As the FC power it fixed at 120 W throughout the period, rest of the load power along with the transient, is supplied by the battery. Thus, the battery current changes from initial 1.69 to 7 A and back again to 1.69 A, during this load change, to maintain the load side dc bus voltage at 220 V. During the load change a voltage overshoot and undershoot of $\pm 0.9\%$ are observed with settling time of 50 ms. Fig. 14(b) verifies that during this dynamic load change the duty ratio controller is not affected by the phase shift controller and load transient. Thus, the input clamp capacitor voltages (voltages appearing across the transformer windings) are fixed at their respective rated voltage levels.

The proposed control system is further verified for a constant load of 176 W with a step-change in the FC current reference from 3.2 to 4.8 A and vice versa. In this case, the FC current controller performance is verified with a step-changing FC current reference. At the same time, the load voltage controller performance is also verified, for its effectiveness in maintaining the load voltage constant at 220 V in spite of the source current change. Fig. 15(a) shows that, during FC current variation (decided by the FC current controller), the battery current (decided by the load voltage controller) adjusts accordingly in order to maintain the load voltage fixed. Fig. 15(b) verifies the duty

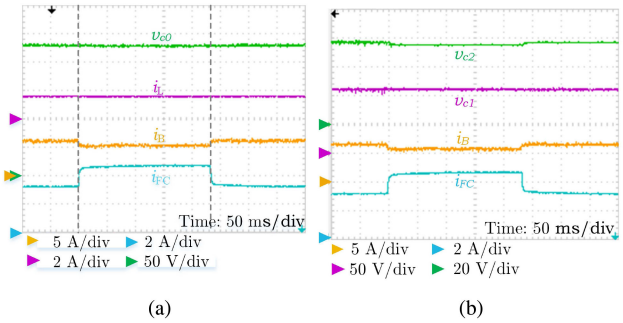

Fig. 15. Closed-loop performance of the proposed PI-based decoupled controller for FC current change. (a) Change in FC current from 3.2 to 4.8 A and back for a fixed load power $P_0 = 176$ W, $V_{FC} = 24$ V, $V_B = 45$ V. (b) Input clamp capacitor voltages variation with source current profile.

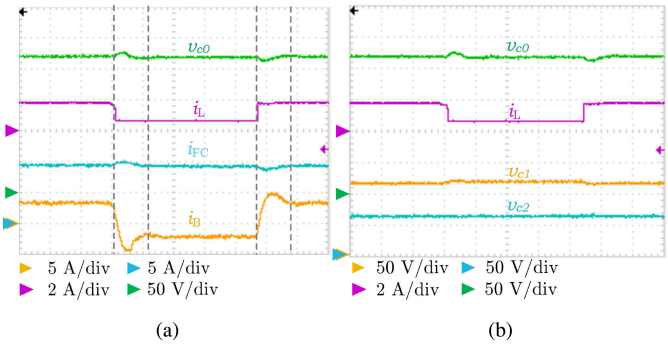

Fig. 16. Closed-loop performance of the proposed PI-based decoupled controller during power reversed transient (negative battery current). (a) Change in load power from 418 to 132 W and back to 418 W, for a fixed FC current of 9.5 A $V_{FC} = 28.3$ V, $V_B = 49$ V. (b) Input and output clamp capacitor voltage variations with load current profile.

ratio control scheme, by ensuring constant source side clamp capacitor voltages, despite sudden source current variation.

The controller performance is also verified for the case of power reversal, which basically verifies the bidirectional power flow capability of the system. To do that, load power is decreased in a step from 418 to 132 W and again increased to 418 W in another step. During this load change, the FC current was controlled at a fixed value of 9.5 A, corresponding to FC power of 269 W, as seen from Fig. 16(a). During the whole event the load voltage was maintained at its rated value of 220 V, by the load voltage controller. As the FC power is constant at 269 W, the load transient is handled by the battery. When the load power is more (418 W) than the FC power (269 W), the battery supplies 3.8 A at a battery voltage of 49 V. As the FC power is kept fixed at 269 W, during load decrease, the battery starts charging with a current of 2 A (battery current direction reversed), to maintain the power balance. This further verifies the flexibility of the designed controller during power reversal. Fig. 16(b) shows that, in spite of the battery current transient, the input side dc bus voltages are still maintained at their rated voltages. In Table IV, a control performance comparison among various three-port converters available in the literature is made with the proposed control scheme. It shows that the proposed decoupled controller reduces the load voltage overshoot/undershoot significantly with moderate settling time.

TABLE IV
COMPARISON OF DYNAMIC RESPONSE WITH OTHER THREE PORT CONVERTERS

Ref.	Voltage(V) Power(W)*	Load Change**	Overshoot/ Undershoot(%)	Settling Time (ms)
[24]	400V, 200W	50%-100%	5	200
[25]	300V, 500W	***	0.9	22
[26]	100V, 400W	25%-50%	4	80
[27]	380V, 3.5kW	50%-100%	3.4	13
[28]	400V, 1kW	80%-100%	1.3	250
[29]	400V, 1kW	16%-58%	5	200
Proposed Work	220V, 1kW	20%-44%	0.9	50

*Rated load voltage and load power rating of converters.
**Load change calculated with respect to the rated powers of the converter.
***Load change information not provided.

VI. CONCLUSION

A detailed modeling and controller design technique is proposed for a full-bridge CF-TAB-based MPC considering its full control flexibility. The proposed modeling techniques reduces the complexity involved with TAB-based systems controller design, irrespective of the TAB structure (VF/CF-TAB), modulation scheme, transformer voltage wave shape, and converter operating region. The proposed small-signal model is used to design two different controllers, namely the state feedback controller and the PI-based decoupled controller. The proposed PI-based decoupled controller reduces the highly coupled TAB model to three lower order ac equivalent circuits, which reduces design complexity significantly. Also, it provides better transient performance in terms of reduced peak voltage overshoot/undershoot with lower settling time compared to the state feedback approach (Simulation results presented in this regard are supported by the available recent literature) with simple structure. But, for a generalized MPC converter involving more number of active bridges and control variables, the PI-based approach may not be suitable due to the difficulty involved in finding a suitable decoupling matrix. In view of that, state feedback control can be a promising solution for a more generalized MPC structure.

REFERENCES

[1] H. Tao, A. Kotsopoulos, J. L. Duarte, and M. A. M. Hendrix, "Family of multiport bidirectional dc-dc converters," *IEE Proc. - Electric Power Appl.*, vol. 153, no. 3, pp. 451–458, May 2006.
[2] Z. Rehman, I. Al-Bahadly, and S. Mukhopadhyay, "Multiinput dc-dc converters in renewable energy applications–an overview," *Renew. Sustain. Energy Rev.*, vol. 41, pp. 521–539, 2015.
[3] D. Sha, X. Wang, and D. Chen, "High-efficiency current-fed dual active bridge DC-DC converter with ZVS achievement throughout full range of load using optimized switching patterns," *IEEE Trans. Power Electron.*, vol. 33, no. 2, pp. 1347–1357, Feb. 2018.
[4] D. Sha, Y. Xu, J. Zhang, and Y. Yan, "Current-fed hybrid dual active bridge DC-DC converter for a fuel cell power conditioning system with reduced input current ripple," *IEEE Trans. Ind. Electron.*, vol. 64, no. 8, pp. 6628–6638, Aug. 2017.
[5] Z. Ding, C. Yang, Z. Zhang, C. Wang, and S. Xie, "A novel soft-switching multiport bidirectional dc-dc converter for hybrid energy storage system," *IEEE Trans. Power Electron.*, vol. 29, no. 4, pp. 1595–1609, Apr. 2014.

[6] N. Zhang, D. Sutanto, and K. M. Muttaqi, "A review of topologies of three-port dc-dc converters for the integration of renewable energy and energy storage system," *Renew. Sustain. Energy Rev.*, vol. 56, pp. 388–401, 2016.
[7] M. Neubert, A. Gorodnichev, J. Gottschlich, and R. W. De Doncker, "Performance analysis of a triple-active bridge converter for interconnection of future dc-grids," in *Proc. IEEE Energy Convers. Congr. Expo.*, Sep. 2016, pp. 1–8.
[8] V. N. S. R. Jakka, A. Shukla, and S. V. Kulkarni, "Flexible power electronic converters for producing ac superimposed dc (ACSDC) voltages," *IEEE Trans. Ind. Electron.*, vol. 65, no. 4, pp. 3145–3156, Apr. 2018.
[9] M. Phattanasak, R. Gavagsaz-Ghoachani, J. Martin, B. Nahid-Mobarakeh, S. Pierfederici, and B. Davat, "Control of a hybrid energy source comprising a fuel cell and two storage devices using isolated three-port bidirectional dc-dc converters," *IEEE Trans. Ind. Appl.*, vol. 51, no. 1, pp. 491–497, Jan. 2015.
[10] K. Kurosawa, K. Nishimoto, K. Katagiri, J. Arai, P. Huang, and Y. Kado, "Smart self-charging method implemented in a triple-active-bridge converter," in *Proc. 20th Eur. Conf. Power Electron. Appl.*, Sep. 2018, pp. P.1–P.9.
[11] D. Liu and H. Li, "A zvs bi-directional dc-dc converter for multiple energy storage elements," *IEEE Trans. Power Electron.*, vol. 21, no. 5, pp. 1513–1517, Sep. 2006.
[12] L. Wang, Z. Wang, and H. Li, "Asymmetrical duty cycle control and decoupled power flow design of a three-port bidirectional dc-dc converter for fuel cell vehicle application," *IEEE Trans. Power Electron.*, vol. 27, no. 2, pp. 891–904, Feb. 2012.
[13] S. Chakraborty and S. Chattopadhyay, "Operation of a triple-active-bridge-based battery-integrated isolated pv microinverter," in *Proc. 43rd Annu. Conf. IEEE Ind. Electron. Soc.*, Oct. 2017, pp. 2611–2616.
[14] H. Tao, J. L. Duarte, and M. A. M. Hendrix, "Three-port triple-half-bridge bidirectional converter with zero-voltage switching," *IEEE Trans. Power Electron.*, vol. 23, no. 2, pp. 782–792, Mar. 2008.
[15] R. Chattopadhyay, G. Gohil, S. Acharya, V. Nair, and S. Bhattacharya, "Efficiency improvement of three port high frequency transformer isolated triple active bridge converter," in *Proc. IEEE Appl. Power Electron. Conf. Expo.*, Mar. 2018, pp. 1807–1814.
[16] H. Tao, A. Kotsopoulos, J. L. Duarte, and M. A. M. Hendrix, "Transformer-coupled multiport ZVS bidirectional dc-dc converter with wide input range," *IEEE Trans. Power Electron.*, vol. 23, no. 2, pp. 771–781, Mar. 2008.
[17] Y. Tran, F. D. Freijedo, and D. Dujic, "Open-loop power sharing characteristic of a three-port resonant LLC converter," *CPSS Trans. Power Electron. Appl.*, vol. 4, no. 2, pp. 171–179, Jun. 2019.
[18] M. Grabarek, M. Parchomiuk, and R. Strzelecki, "Conjugated control of triple active bridge converter with common HFT," in *Proc. 11th IEEE Int. Conf. Compat., Power Electron. Power Eng.*, Apr. 2017, pp. 304–307.
[19] K. Nishimoto, Y. Kado, R. Kasashima, S. Nakagawa, and K. Wada, "Decoupling power flow control system in triple active bridge converter rated at 400 v, 10 kw, and 20 khz," in *Proc. IEEE 8th Int. Symp. Power Electron. Distrib. Gener. Syst.*, Apr. 2017, pp. 1–6.
[20] R. Kasashima, S. Nakagawa, K. Nishimoto, Y. Kado, and K. Wada, "Implementation and power-loss characteristics of 400-v, 10-kw, 20-khz three-way isolated dc/dc converter as a power routing unit for constructing microgrid systems," in *Proc. IEEE Region ten Conf.*, Nov. 2016, pp. 793–796.
[21] T. Ohno and N. Hoshi, "A new control method for triple-active bridge converter with feed forward control," in *Proc. Int. Power Electron. Conf.*, May 2018, pp. 971–976.
[22] J. You, M. Vilathgamuwa, N. Ghasemi, and B. Gong, "Elimination of current oscillation in isolated three-port power converters using active damping method," *IET Power Electron.*, vol. 12, no. 11, pp. 2802–2809, 2019.
[23] I. Biswas, D. Kastha, and P. Bajpai, "Tab based multiport converter with optimized transformer rms current and improved ZVS range for dc microgrid applications," in *Proc. 45th Annu. Conf. IEEE Ind. Electron. Soc.*, vol. 1, Oct. 2019, pp. 2050–2055.
[24] S. Salehi Dobakhshari, S. H. Fathi, and J. MiliMonfared, "A new fully soft-switched three-port dc/dc converter with high voltage gain and reduced number of semiconductors for hybrid energy applications," *IEEE Trans. Power Electron.*, vol. 35, no. 4, pp. 3590–3600, Apr. 2020.
[25] H. Wu, J. Zhang, X. Qin, T. Mu, and Y. Xing, "Secondary-side-regulated soft-switching full-bridge three-port converter based on bridgeless boost rectifier and bidirectional converter for multiple energy interface," *IEEE Trans. Power Electron.*, vol. 31, no. 7, pp. 4847–4860, Jul. 2016.
[26] H. Wu, K. Sun, L. Zhu, and Y. Xing, "An interleaved half-bridge three-port converter with enhanced power transfer capability using three-leg rectifier for renewable energy applications," *IEEE J. Emerg. Sel. Topics Power Electron.*, vol. 4, no. 2, pp. 606–616, Jun. 2016.
[27] R. N. M. de Oliveira, L. C. dos Santos Mazza, H. M. de Oliveira Filho, and D. d. S. Oliveira, "A three-port isolated three-phase current-fed DC-DC converter feasible to pv and storage energy system connection on a dc distribution grid," *IEEE Trans. Ind. Appl.*, vol. 55, no. 5, pp. 4910–4919, Sep. 2019.
[28] H. Moradisizkoohi, N. Elsayad, M. Shojaie, and O. A. Mohammed, "PWM plus phase-shift-modulated three-port three-level soft-switching converter using GAN switches for photovoltaic applications," *IEEE J. Emerg. Sel. Topics Power Electron.*, vol. 7, no. 2, pp. 636–652, Jun. 2019.
[29] P. Wang, P. Ren, X. Lu, W. Wang, and D. Xu, "Topology analysis and power sharing control of a two-stage three-port hybrid energy storage converter for dc microgrids," *IEEE J. Emerg. Sel. Topics Power Electron.*, to be published, doi: 10.1109/JESTPE.2019.2947249.

Ishita Biswas (Student Member, IEEE) received the B.Tech. degree in electrical engineering from West Bengal University of Technology, Kolkata, India, in 2011, and the M.S degree in electrical engineering (with specialization in power and energy system) in 2015 from the Indian Institute of Technology Kharagpur, Kharagpur, India, where she is currently working toward the Ph.D. degree with the Department of Electrical Engineering.

Her research interests include topologies and control of multiport dc-dc converter and high gain dc-dc converter.

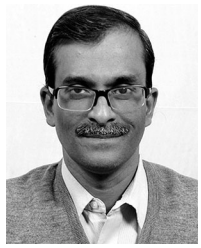

Debaprasad Kastha (Senior Member, IEEE) received the B.E. degree in electrical engineering from the Indian Institute of Engineering Science and Technology (formerly Bengal Engineering College, Calcutta University, Kolkata), Shibpur, India, in 1987, the M.E. degree in electrical engineering (with specialization in power electronics) from the Indian Institute of Science, Bangalore, India, in 1989, and the Ph.D. degree from the University of Tennessee, Knoxville, TN, USA, in 1993.

From March 1989 to December 1989, he was with the Research and Development (Electronics) Division, Crompton Greaves, Ltd., Mumbai, India. In 1994, he joined the Department of Electrical Engineering, Indian Institute of Technology, Kharagpur, India, where he became a Professor in 2011. He has been teaching and doing research in the area of power electronics and drives for more than two decades now and has authored about 50 technical papers, books, and electronic teaching aids. His research interests include the areas of wind power generation, machine drives, dc power supply and distribution systems. He has coauthored a book titled *Wind Electrical Systems* (Oxford University Press) and prepared web-based and video courses on power electronics and electrical machines, respectively, as parts of NPTEL program of Government of India.

Prabodh Bajpai (Senior Member, IEEE) received the B.E. degree in electrical engineering from the University of Roorkee [now Indian Institute of Technology (IIT) Roorkee], Roorkee, India, in 1997, the M.Tech. degree in energy studies from IIT Delhi, New Delhi, India, in 2001, and the Ph.D. degree in electrical engineering from IIT Kanpur, Kanpur, India, in 2008.

He is currently working as an Associate Professor with the Department of Electrical Engineering, IIT Kharagpur, Kharagpur, India. His research interests include power system restructuring, renewable energy systems, and power system optimization, multiport converters.

Dr. Bajpai was awarded BASE Fellowship from DST, MHRD India towork at the University of Washington, Seattle, WA, USA, in 2015.